Extended quantitative rescattering model for simulating high-order harmonic streaking spectra by synchronization of an intense IR laser and a time-delayed attosecond XUV pulse

Kan Wang, Baochang Li, Xiangyu Tang, Chenhui Xu, C. D. Lin, and Cheng Jin

Phys. Rev. A **104**, 033102 — Published 1 September 2021

DOI: 10.1103/PhysRevA.104.033102

Extended quantitative rescattering model for simulating high-order harmonic streaking spectra by synchronization of an intense IR laser and a time delayed attosecond XUV pulse

Kan Wang,[1] Baochang Li,[1] Xiangyu Tang,[1] Chenhui Xu,[1] C. D. Lin,[2] and Cheng Jin[1,*]

[1]*Department of Applied Physics, Nanjing University of Science and Technology, Nanjing, Jiangsu 210094, China*
[2]*J. R. Macdonald Laboratory, Department of Physics, Kansas State University, Manhattan, Kansas 66506, USA*

(Dated: August 18, 2021)

We theoretically investigate the modulated high harmonic generation (HHG) driven by an intense few-cycle infrared (IR) laser field and a weak extreme ultraviolet (XUV) pulse at a delayed time. We establish an extended quantitative rescattering (EQRS) model to simulate the HHG streaking spectra, with the ideas of correcting the IR ionization and the transition from the ground to continuum states in the strong-field approximation. The EQRS model has an accuracy comparable to that by "exactly" solving the time-dependent Schrödinger equation (TDSE). We reveal that the fringes in the streaking spectra are caused by the interference between the attosecond XUV pulse and harmonics resulted from different recombination pathways under the intense IR laser. We then demonstrate that the XUV pulse can be accurately retrieved by treating the single-atom TDSE results or macroscopic propagation results as the "input" data. This work provides with a tool for efficiently simulating and through analyzing the XUV-assisted HHG, which could also enhance its capability for tracing the electron dynamics involved in the strong-field phenomena.

I. INTRODUCTION

Laser-driven high harmonic generation (HHG) has received continuous research interest in the past thirty years since the first observations at the end of 1980's [1, 2]. HHG is fundamental to attosecond science [3–5] as it has become a reliable source for producing ultrashort attosecond light pulses in the form of attosecond pulse trains (APTs) [6] or isolated attosecond pulses (IAPs) [7]. With the idea of restricting the efficient HHG emission occurring in a short time interval, various generation techniques have been developed to produce IAPs with durations of few hundreds to few tens attoseconds in the extreme ultraviolet (XUV) based on the traditional Ti:sapphire laser. These include amplitude gating [8], ionization gating [9], polarization gating [10], attosecond lighthouse [11, 12], multi-color waveform synthesis [13–16], etc. Such attosecond XUV pulses provide with a unique tool for probing the electron dynamics with time-resolved spectroscopy [17, 18], initiating the electron ionization [19, 20], modifying the trajectory of electron under the infrared (IR) laser [21], and so on.

The synchronization of attosecond XUV pulses and the IR laser has been widely used to perturb or to reform the IR-generated HHG spectra by varying the time delay between the XUV pulse and IR laser. The XUV field was employed to populate the electron to the excited states or to select a specific electron trajectory by controlling the ionization step, thus greatly enhancing the yield of IR-induced HHG [22–24]. The HHG plateau by the IR laser was extended by the addition of a weak XUV pulse due to the XUV field-induced ac-Stark modulations of the ground state [25]. The extension of HHG plateau can also be achieved by adding XUV pulses with higher photon energies, which enables the inner-shell electrons involving in the HHG process [26, 27]. It has been shown that the interaction of XUV field and IR laser can significantly influence one of three steps in the HHG process. If this interaction happens at ionization step, the IR tunneling ionization is suppressed because the ionization energy of target is effectively increased [28]. If this interaction occurs at propagation step, the multiple rescattering of the active electron can be induced, which is important for low-energy harmonics [29, 30]. When the photon energy of XUV pulse is far from the ionization threshold, it can be forward scattered from the non-stationary electronic wave packet promoted by the intense IR laser at the recombination step, thus leading to the parametric amplification of XUV pulse, which has been extensively examined both experimentally and theoretically [31–39]. The XUV-assisted HHG has also been proposed to characterize attosecond pulses. For example, Xue *et al.* [40] theoretically investigated the dependence of the spectrum modulation on the chirp of the XUV under the synchronized XUV and IR laser pulses, which could be useful for the reconstruction of XUV spectral phase. Sarantseva *et al.* [41] proposed to retrieve the temporal intensity profile of an XUV attosecond pulse based on the XUV-assisted HHG by an intense IR pulse. Very recently, Dong et al. [42] found that interference fringe structures in the HHG streaking spectra can be used to observe the interplay of the photoionization and tunneling ionization electron dynamics in attosecond resolution. Sarantseva *et al.* [43] proposed a method for direct reconstruction of the HHG time-frequency spectrogram using a time-delayed XUV-assisted HHG spectra.

*cjin@njust.edu.cn

In these studies, the HHG streaking spectra by the combination of XUV pulse and IR laser are usually computed quantum mechanically by solving the time-dependent Schrödinger equation (TDSE) under the single-active electron (SAE) approximation [21, 42, 43], or by employing the formulation of strong-field approximation (SFA) [29]. It is well known that TDSE can give precise results, but the physical mechanism has been hid behind the numerical spectra. On the contrary, in the SFA the analytical formula can offer the physical meaning to describe the XUV-assisted HHG process, but it cannot simulate the spectra precisely. Therefore, the physical mechanism of XUV-assisted HHG remains insufficiently explored. It is necessary to develop new approaches to precisely simulate the HHG streaking spectra and to reveal the generation mechanism.

In this work, our main goal is to develop a theoretical method to accurately simulate the HHG streaking spectra. We choose a weak IAP pulse with its central photon energy being far from the ionization threshold of target atom, which is used to modulate the continuum harmonic spectrum in the cutoff region generated by an intense few-cycle IR laser. The spectral modulation can be controlled by adjusting the time delay between the XUV and IR laser pulses. We will first separate the coupling between the XUV and IR pulses in the formulation of the strong-field approximation (SFA), and then we will extend and modify the well established quantitative rescattering (QRS) model [44–46], which is valid for HHG from linearly polarized single- or multi-color IR laser pulses [47–49]. The calculated streaking spectra will be compared to those obtained by numerically solving the TDSE. Next, we will explain the interference fringes in the streaking spectra and uncover their physical origin. Then, we will demonstrate that by taking the TDSE results as "input" data and taking into account of macroscopic propagation effects, the HHG streaking spectra can be employed to recover the information of the input attosecond XUV pulse.

II. THEORETICAL METHODS

A. Separation of the contributions of IR and XUV pulses to the induced dipole in the strong field approximation

We first use the strong-field approximation (SFA) [29] to calculate the HHG streaking spectra under the linearly polarized XUV and the intense IR laser pulses. The single-atom induced dipole along the polarization direction at a fixed time delay τ between the two pulses can be expressed as

$$\begin{aligned} x(t,\tau) &= i\int_0^t dt' \left(\frac{\pi}{\varepsilon + i(t-t')}\right)^{3/2} \\ &\times d^*[p_{st}(t,t') - A(t)] e^{-iS_{st}(t,t')} d[p_{st}(t,t') - A(t')] \\ &\times E(t') + c.c., \end{aligned} \tag{1}$$

where $E(t) = E_{IR}(t) + E_{XUV}(t-\tau)$ is the combined electric field of IR and XUV pulses, and $A(t) = A_{IR}(t) + A_{XUV}(t-\tau)$ is the corresponding vector potential. Note that negative τ means the XUV pulse comes earlier than the peak of IR laser. Since the continuum state is treated as plane wave, the dipole transition matrix element from the ground state to the continuum state can be expressed as

$$d(p) = f(p) \cdot p, \tag{2}$$

where p is the electron momentum, and $f(p)$ is a complex function of p. Since the XUV is quite weak compared to the IR laser to isolate the induced dipole by the IR laser alone, $E(t) \approx E_{IR}(t)$ and $f(p_{st} - A(t)) \approx f(p_{st} - A_{IR}(t))$, thus Eq. (1) can be expressed as

$$\begin{aligned} x(t,\tau) &= i\int_0^t dt' \left(\frac{\pi}{\varepsilon + i(t-t')}\right)^{3/2} \\ &\times f^*[p_{st}(t,t') - A_{IR}(t)] e^{-iS_{st}(t,t')} f[p_{st}(t,t') - A_{IR}(t')] \\ &\cdot [p_{st}(t,t') - A_{IR}(t) - A_{XUV}(t-\tau)] \\ &\cdot [p_{st}(t,t') - A_{IR}(t') - A_{XUV}(t'-\tau)] \\ &\times E_{IR}(t') + c.c., \end{aligned} \tag{3}$$

where p_{st} is the stationary momentum and S_{st} is the corresponding stationary action defined in the SFA [29]. The validity of Eq. (3) has been checked by comparing with the HHG results from standard SFA in Eq. (1).

To separate different processes in the time-dependent dipole, we rewrite $x(t,\tau)$ as

$$x(t,\tau) = x_1(t) + x_2(t,\tau) + x_3(t,\tau) + x_4(t,\tau). \tag{4}$$

Each term in the right hand of the equation can be explicitly expressed in the following:

$$\begin{aligned} x_1(t) &= i\int_0^t dt' \left(\frac{\pi}{\varepsilon + i(t-t')}\right)^{3/2} \\ &\times f^*[p_{st}(t,t') - A_{IR}(t)] e^{-iS_{st}(t,t')} f[p_{st}(t,t') - A_{IR}(t')] \\ &\cdot [p_{st}(t,t') - A_{IR}(t)][p_{st}(t,t') - A_{IR}(t')] \\ &\times E_{IR}(t') + c.c., \end{aligned} \tag{5}$$

$$\begin{aligned} x_2(t,\tau) &= -i\int_0^t dt' \left(\frac{\pi}{\varepsilon + i(t-t')}\right)^{3/2} \\ &\times f^*[p_{st}(t,t') - A_{IR}(t)] e^{-iS_{st}(t,t')} f[p_{st}(t,t') - A_{IR}(t')] \\ &\cdot [p_{st}(t,t') - A_{IR}(t)] A_{XUV}(t'-\tau) \\ &\times E_{IR}(t') + c.c., \end{aligned} \tag{6}$$

$$\begin{aligned} x_3(t,\tau) &= -i\int_0^t dt' \left(\frac{\pi}{\varepsilon + i(t-t')}\right)^{3/2} \\ &\times f^*[p_{st}(t,t') - A_{IR}(t)] e^{-iS_{st}(t,t')} f[p_{st}(t,t') - A_{IR}(t')] \\ &\cdot A_{XUV}(t-\tau)[p_{st}(t,t') - A_{IR}(t')] \\ &\times E_{IR}(t') + c.c., \end{aligned} \tag{7}$$

and

$$x_4(t,\tau) = i\int_0^t dt' \left(\frac{\pi}{\varepsilon + i(t-t')}\right)^{3/2} \times f^*[p_{st}(t,t') - A_{IR}(t)]e^{-iS_{st}(t,t')} f[p_{st}(t,t') - A_{IR}(t')] \cdot A_{XUV}(t-\tau)A_{XUV}(t'-\tau) \times E_{IR}(t') + c.c. \quad (8)$$

Note that similar formulation in Eq. (4) has been used by Serrat *et al.* [32, 33]. The limitation of SFA for describing the single-atom response of HHG is well known. We will correct each term in Eq. (4) individually.

B. The QRS model for the induced dipole by the IR laser alone

The $x_1(t)$ in Eq. (5) doesn't depend on the time delay τ. It can be rewritten as

$$x_1(t) = i\int_0^t dt' \left(\frac{\pi}{\varepsilon + i(t-t')}\right)^{3/2} \times d^*[p_{st}(t,t') - A_{IR}(t)]e^{-iS_{st}(t,t')} d[p_{st}(t,t') - A_{IR}(t')] \times E_{IR}(t') + c.c. \quad (9)$$

This is the single-atom induced dipole driven by the IR laser alone. In the frequency domain, according to the quantitative rescatterring (QRS) model [50], it can be expressed as

$$x_1^{\rm SFA}(\omega, I) = N^{\rm SFA}(I)^{1/2} W_1(\omega) d^{\rm SFA}(\omega), \quad (10)$$

where $N^{\rm SFA}(I)$ and $d^{\rm SFA}(\omega)$ are the ionization probability (usually taken at the end of the IR laser pulse) and the transition dipole moment calculated within the SFA, respectively. Note that $d(\omega) = \langle 0|\,\vec{x}\,|p\rangle$, where $\omega = I_p + p^2/2$ (atomic units) with electron position operator $\vec{x}$ (along laser polarization direction), ionization potential I_p and wave functions of ground state $|0\rangle$ and continuum states $|p\rangle$. The explicit expressions of $d^{\rm SFA}(\omega)$ are given in Eqs. (16) and (19). The dependence of the induced dipole on the peak intensity I of the IR laser has been given explicitly. In Eq. (10), the SFA can only give the correct electron wave packet $W_1(\omega)$ as

$$W_1(\omega) = \frac{x_1^{\rm SFA}(\omega, I)}{N^{\rm SFA}(I)^{1/2} d^{\rm SFA}(\omega)}, \quad (11)$$

thus the QRS obtains the accurate induced dipole in the following:

$$x_1^{\rm QRS}(\omega, I) = x_1^{\rm SFA}(\omega, I)\frac{N^{\rm QRS}(I)^{1/2}}{N^{\rm SFA}(I)^{1/2}}\frac{d^{\rm QRS}(\omega)}{d^{\rm SFA}(\omega)}. \quad (12)$$

Here the ionization probability $N^{\rm QRS}(I)$ can be calculated by using the PPT model [51], and $d^{\rm QRS}(\omega)$ is computed by using the "exact" wave function for the bound and continuum states within the single-active electron (SAE) approximation. The QRS model has been well established by calibrating against HHG results from TDSE calculations for atomic targets [46–48] and simple molecules [44, 45, 49]. The factorization of induced dipole moment has also been derived analytically by others [52–55]. In this work, our target atom is Ne, and its model potential is given in Ref. [56].

C. Corrections of the XUV and IR coupling terms by extending the QRS model

For the $x_2(t,\tau)$ and $x_3(t,\tau)$ terms in Eq. (5), the interactions of XUV pulse and IR laser with the atom are coupled. Similar to $x_1(\omega)$, in the frequency domain, $N(I)$ and $d(\omega)$ are the key factors to construct $x_2(\omega,\tau)$ and $x_3(\omega,\tau)$. Therefore, we take advantage of factorization idea in the QRS, and write these terms at time delay τ in a similar way as

$$x_{2,3}^{\rm SFA}(\omega, I, \tau) = N^{\rm SFA}(I)^{\alpha} W_{2,3}(\omega,\tau)|d^{\rm SFA}(\omega)|^{\beta}, \quad (13)$$

where $W_{2,3}(\omega,\tau)$ are complex quantities similar to the electron wave packet in $x_1(\omega)$ and depends on the external field only. The parameters α and β are to be determined by fitting from the SFA expressions. Once these parameters are known, $W_{2,3}(\omega,\tau)$ can be obtained, and accurate $x_2(\omega,\tau)$ and $x_3(\omega,\tau)$ are calculated by the extended quantitative rescattering (EQRS) model as

$$x_{2,3}^{\rm EQRS}(\omega, I, \tau) = x_{2,3}^{\rm SFA}(\omega, I, \tau)\frac{N^{\rm QRS}(I)^{\alpha}}{N^{\rm SFA}(I)^{\alpha}}\frac{|d^{\rm QRS}(\omega)|^{\beta}}{|d^{\rm SFA}(\omega)|^{\beta}}. \quad (14)$$

Since in Eq. (8) the term $A_{XUV}(t-\tau)A_{XUV}(t'-\tau)$ is much smaller than the terms of $[p_{st}(t,t') - A_{IR}(t)]A_{XUV}(t'-\tau)$ and $A_{XUV}(t-\tau)[p_{st}(t,t') - A_{IR}(t')]$ in $x_2(t,\tau)$ and $x_3(t,\tau)$, respectively, the $x_4(t,\tau)$ is neglected in $x(t,\tau)$. Thus, in the EQRS model, the improved induced dipole by the XUV and IR pulses at a time-delay τ can be computed from

$$x^{\rm EQRS}(\omega, I, \tau) = x_1^{\rm QRS}(\omega, I) + x_2^{\rm EQRS}(\omega, I, \tau) + x_3^{\rm EQRS}(\omega, I, \tau). \quad (15)$$

III. RESULTS AND DISCUSSION

A. The validity of the EQRS model for obtaining the HHG streaking spectra

1. *The fitting procedure for determining the power factors in the EQRS model*

In this work, we are interested in the spectral region where the XUV pulse overlaps with the high harmonics generated by the IR laser. To determine the power factors α and β in Eq. (13), we fit them from the calculated $x_{2,3}^{\rm SFA}(\omega, I, \tau)$. In the calculation, we treat Ne as

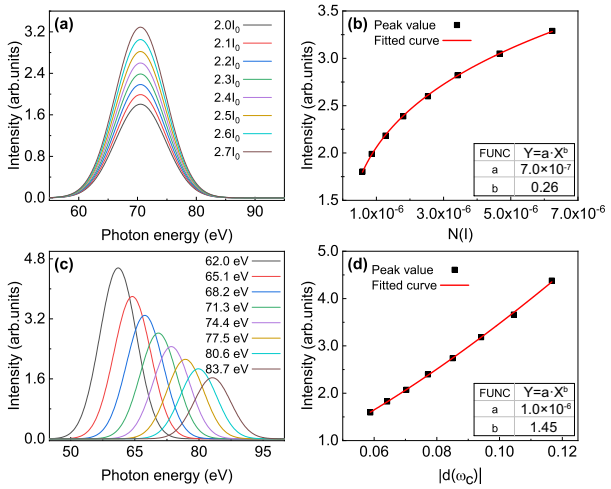

FIG. 1: (a) The spectra of $|x_2^{\rm SFA}(\omega, I, \tau)|^2$ calculated at different IR intensities indicated in units of I_0, where I_0=10^{14} W/cm^2. The peak value is gradually increased with the increase of the IR intensity. Their peak values (black-squares) and the fitting curve (red line) as a function of $N(I)$ are shown in (b). (c) The spectra of $|x_2^{\rm SFA}(\omega, I, \tau)|^2$ at different XUV central photon energies. The peak position coincides with the central energy of the XUV as labeled in the figure. Their peak values (black-squares) and the fitted curve (red line) with $|d(\omega_c)|$ are shown in (d). The insets show the form of power law fitting functions and the fitted parameters.

a hydrogenlike atom. Then the transition dipole is given by

$$d(p) = i\frac{2^{7/2}(2I_p)^{5/4}}{\pi}\frac{p}{(p^2+2I_p)^3}, \qquad (16)$$

where I_p is the ionization potential of Ne. We set time delay $\tau = 0$, XUV pulse duration as 200 as, central photon energy at 71.3 eV, and peak intensity at 5.0×10^{10} W/cm^2. The IR peak intensity is varied from 2.0 to 2.7 $\times$ 10^{14} W/cm^2. Other IR parameters are: central wavelength of 800 nm, pulse duration of 5 fs (full width at half maximum, FWHM), carrier envelope phase (CEP) of zero, and temporal profile described by a cosine-squared function. The simulated $|x_2^{\rm SFA}(\omega, I, \tau)|^2$ are shown in Fig. 1(a). The spectral shapes are similar except that the peak values increase with intensity, reflecting the increase of ionization probability. In Fig. 1(b), we plot the peak values as a function of the ionization probability $N^{\rm SFA}(I)$ (solid squares). By fitting these data to a power law, the obtained power factor is 0.26 which is close to 1/4. We thus set $\alpha = 1/8$ in Eq. (13). We next fix the intensity at 2.5×10^{14} W/cm^2, and vary the central energy of the XUV pulse from 62.0 to 83.7 eV. The calculated $|x_2^{\rm SFA}(\omega, I, \tau)|^2$ are plotted in Fig. 1(c). The shape of each spectrum is the same, but the peak value and central photon energy are different because of the shift of the central photon energy of XUV pulse, which can be related to the photon-energy dependent transition dipole moment. We apply the central momentum approximation, i.e., $d(\omega)$ is replaced by $d(\omega_c)$, where ω_c is the XUV central photon energy. The peak values of $|x_2^{\rm SFA}(\omega, I, \tau)|^2$ are plotted as a function of $|d(\omega_c)|$ in Fig. 1(d). By fitting the curve to a power law, the power factor obtained is 1.45, which is close to 3/2, so we take $\beta = 3/4$. Using the same fitting procedure, we have checked that α and β do not change much with the time delay τ.

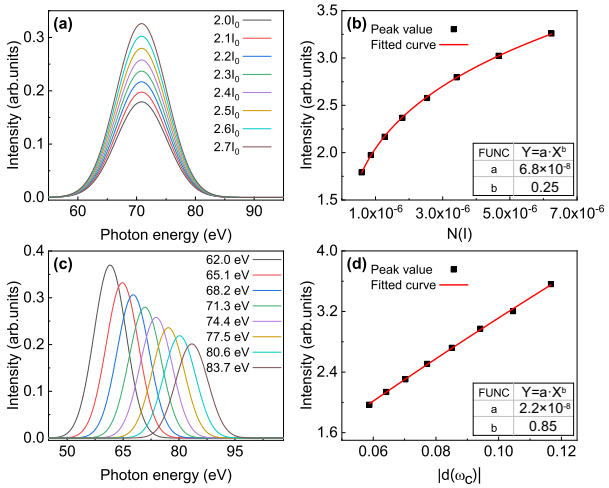

FIG. 2: The same figures as in Fig. 1 except for calculating $|x_3^{\rm SFA}(\omega, I, \tau)|^2$.

We use the same procedure to determine the α and β factors in $x_3^{\rm SFA}(\omega, I, \tau)$. By setting $\tau = 0$, the corresponding figures similar to Fig. 1 are shown in Fig. 2. The fitted power factors are 0.25 and 0.85, or about 1/4 and 4/5 from the figures. Thus $\alpha = 1/8$ and $\beta = 2/5$ in Eq. (13). We have also checked that these parameters do not change with τ.

Thus we obtain

$$x_2^{\rm SFA}(\omega, I, \tau) = N^{\rm SFA}(I)^{1/8} W_2(\omega, \tau)|d^{\rm SFA}(\omega)|^{3/4}, \quad (17)$$

and

$$x_3^{\rm SFA}(\omega, I, \tau) = N^{\rm SFA}(I)^{1/8} W_3(\omega, \tau)|d^{\rm SFA}(\omega)|^{2/5}. \quad (18)$$

Eqs. (17) and (18) give the contribution of XUV pulse to the induced dipole in the presence of the IR laser in the strong-field approximation. Note that there is no re-emission of the XUV photon.

2. *Comparison of HHG streaking spectra by using hydrogenlike and Gaussian atoms*

To check the validity of the above fitting procedure, we also treat Ne atom has a Gaussian potential. In this model, the transition dipole moment is [29]

$$d(p) = i\left(\frac{1}{\pi\alpha}\right)^{3/4}\frac{p}{\alpha}e^{-p^2/2\alpha}, \qquad (19)$$

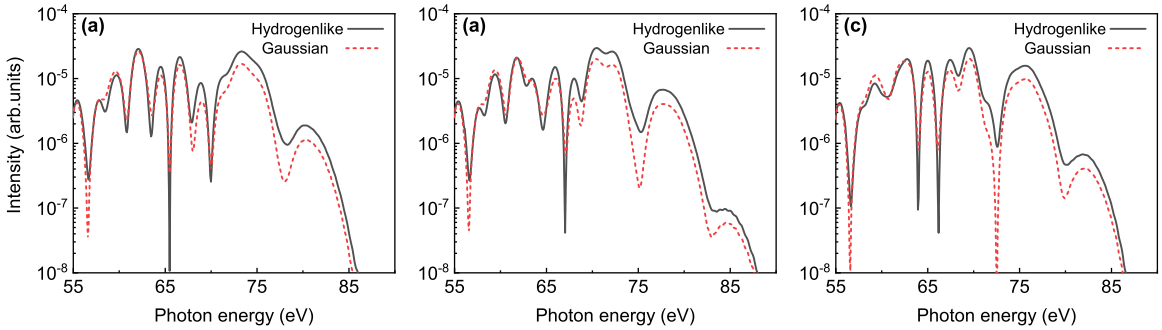

FIG. 3: Comparison of HHG streaking spectra simulated by the EQRS model using hydrogenlike (black full line) and Gaussian model (red dashed line) potential for Ne. The spectra are shown at three selected time delays: (a) 0 as, (b) -20 as, and (c) -40 as.

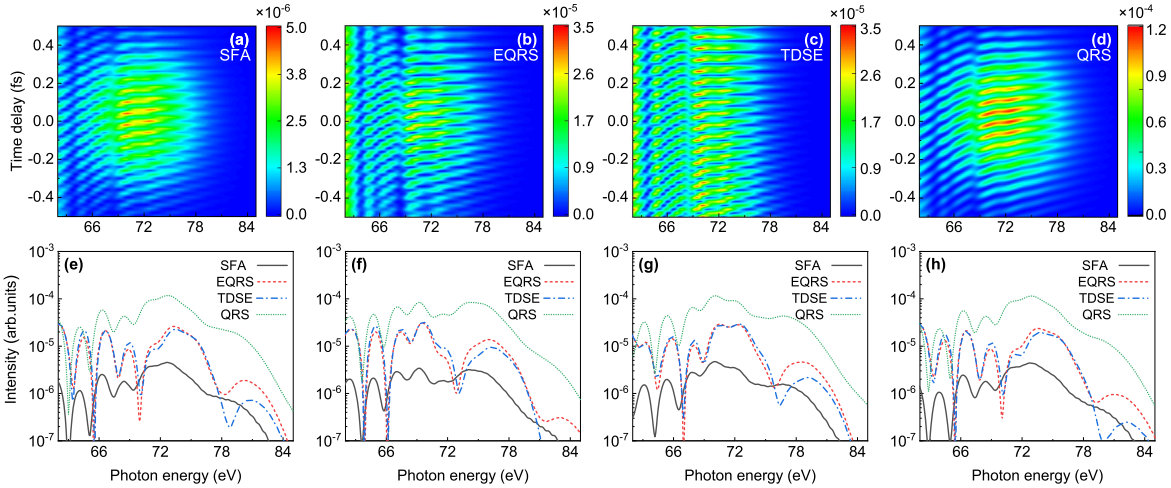

FIG. 4: The HHG streaking spectra calculated by four different methods: (a) SFA (black full line), (b) EQRS (red dashed line), (c) TDSE (blue dot-dashed line), and (d) QRS (green dotted line). Comparison of the spectra obtained by the four methods at time delays of (e) 0 as, (f) 20 as, (g) 40 as, and (h) 60 as.

where $\alpha = 0.7I_p$, with I_p being the ionization potential. We use the same IR and XUV parameters, and the same fitting method, the obtained α and β factors are listed in Table I. One can see the α matches very well for the two different atomic systems while the β values have some differences. Since ionization dominates the contribution to the transition dipole, the difference in β will not much influence the final results of the induced dipole.

TABLE I: The fitted power factors, α and β, in $x_{2,3}(\omega,\tau)$ by using different atomic models

Atomic system	$x_2^{\rm SFA}(\omega,I,\tau)$		$x_3^{\rm SFA}(\omega,I,\tau)$	
	α	β	α	β
Hydrogenlike	1/8	3/4	1/8	2/5
Gaussian	1/8	1/2	1/8	1/4

We consider a 5-fs, 800-nm IR laser with the CEP of 0, and peak intensity of 2.5×10^{14} W/cm^2. This pulse alone can produce high-order harmonics with a cutoff photon energy at about 70 eV. This IR laser is used throughout the rest of this paper unless otherwise stated. We consider a transform-limited (TL) XUV pulse with duration of 200 as, central photon energy of 71.3 eV, and peak intensity of 5×10^{10} W/cm^2. At three time delays of 0, -20, and -40 as, the modulated harmonic spectra calculated by using the EQRS model in Eq. (15) with two different atomic systems are shown in Fig. 3. Here the power spectrum is defined as proportional to $\omega^4|x^{\rm EQRS}(\omega,I,\tau)|^2$ in accordance with the acceleration gauge. One can see that in the spectral region of 55 to 65 eV, the two atomic systems give essentially the same spectra, and between 65 to 85 eV, they differ at most by a factor of 2 while the modulated spectral structures remain identical. This demonstrates that the expressions of $x_{2,3}^{\rm SFA}(\omega,I,\tau)$ in Eq. (13) are universal, and their dependence on the atomic system is quite weak.

B. Comparison of HHG streaking spectra with EQRS, SFA, and TDSE

We next take the same parameters as those in Fig. 3, and calculate the HHG streaking spectra by scanning the time delay from -0.5 fs to 0.5 fs using three methods: SFA, EQRS, and TDSE. The simulated results are shown in Fig. 4. In Figs. 4(a)-(c), all three methods show the modulation versus time delay with a period of about 58 as, which is equal to one optical cycle of the XUV pulse. We also show the HHG streaking spectra obtained directly from the QRS model in Fig. 4(d) to show the necessity of its extension. For the distributions of spectral intensity versus the time delay, the EQRS results are much closer to the TDSE ones in comparison with the SFA ones. The detailed comparison among the four models can be seen in Figs. 4(e)-(h) at four selected time delays. The EQRS can mostly reproduce the modulated HHG spectra by the TDSE over the interested spectral range. However, both the QRS and SFA fails in terms of the spectral shape and intensity. Here the TDSE results obtained under the SAE approximation with the model potential given in Ref. [56] are used to calibrate the EQRS model. The good agreement between them indeed shows the success of our approach for establishing the EQRS model. Note that we have checked that HHG time-frequency spectrogram of Neon in Ref. [43] can also be reproduced by using EQRS model. Compared to solving the TDSE, the computation time of the EQRS model is greatly reduced, and is nearly the same as the calculation time for SFA. Thus, the EQRS model can be used to simulate the HHG streaking spectra. On the other hand, the EQRS model can also be utilized to understand the generation mechanism of XUV-assisted HHG.

C. Interpretation of interference fringes in the HHG streaking spectra

In the HHG streaking spectra, some interference fringes are present as an example replotted in Fig. 5(a) by using EQRS model. A black vertical line is drawn to distinguish the regions of three kinds of interference fringe, and they are with different slopes and are labeled by a black line, a purple line, and a red line, respectively. The photon energy at the white line is 68.9 eV, in coincidence with the cutoff energy of HHG spectrum by the IR laser alone calculated by using $E_c = I_p + 3.17U_p$, where I_p is the ionization potential and U_p is the pondermotive energy. To reveal the origin of interference fringes, we make some assumptions based on the EQRS model, in which the XUV pulse interferes with the harmonics by the IR laser. According to Eq. (15), the intensity of streaking spectra can be expressed as

$$S(\omega,\tau) = |x_1^{\rm QRS}(\omega) + x_2^{\rm EQRS}(\omega,\tau) + x_3^{\rm EQRS}(\omega,\tau)|^2. \quad (20)$$

Since $x_1^{\rm QRS}(\omega)$ is the induced dipole by IR laser and $x_2^{\rm QRS}(\omega)$ and $x_3^{\rm QRS}(\omega)$ are the major and minor contributions to the total induced dipole from the coupled XUV pulse with the IR laser, respectively, we have checked that amplitudes of $x_1^{\rm QRS}(\omega)$ and $x_2^{\rm EQRS}(\omega,\tau)$ are comparable in our simulations, and amplitude of $x_3^{\rm EQRS}(\omega,\tau)$ is smaller compared to that of $x_2^{\rm EQRS}(\omega,\tau)$, which can be neglected in the analysis. We thus have

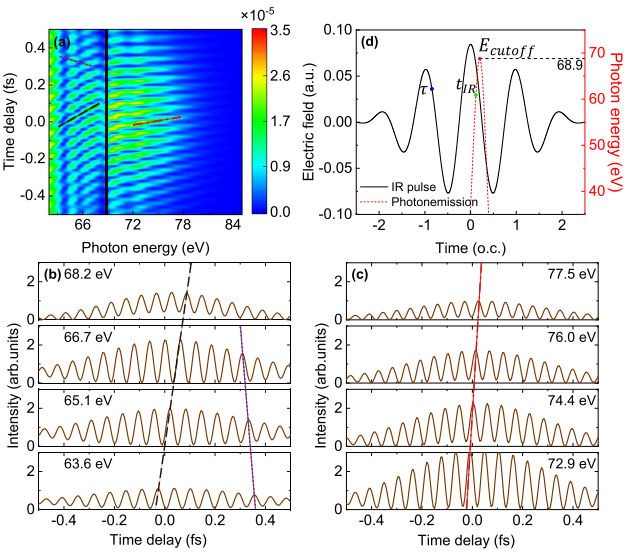

FIG. 5: (a) The HHG streaking spectra calculated by EQRS model, replotted from Fig. 4(b). The vertical (black full) line indicates the cutoff energy E_c by the IR laser, and the slopes of interference fringes are labeled by black dashed, purple dot-dashed, and red dotted lines. The delay-dependent intensity signals of the HHG spectra are shown (b) below and (c) above E_c, respectively. (d) The electric field of IR laser (black full line) and the harmonic emission time as a function of photon energy calculated by the classical trajectory model (red dotted line). t_{IR} is the harmonic emission time, and τ is the time delay between XUV pulse and IR laser.

$$S(\omega,\tau) \approx |A\exp[i\phi_1(\omega)] + A\exp[i\phi_2(\omega,\tau)]|^2, \quad (21)$$

where $\phi_1(\omega)$ is the spectral phase accumulated by the electron along "short" or "long" trajectory under the intense IR laser, and $\phi_2(\omega,\tau) = \omega\tau$ indicating the initial phase of the XUV pulse. Therefore, the modulation of the spectral intensity can be written as

$$S^{mod}(\omega,\tau) \approx A^2\cos[\omega\tau - \phi_1(\omega)]. \quad (22)$$

This equation tells that $\phi_1(\omega)$ can be extracted from the modulated spectra. So the fringes in the HHG streaking spectra reflect the interference between XUV pulse and different HHG pathways through the spectral phase. A time delay in photoemission can be defined as the group delay [57, 58] from the derivative of the spectral phase, which is given by

$$\Delta G = \frac{d\phi_1(\omega)}{d\omega}. \quad (23)$$

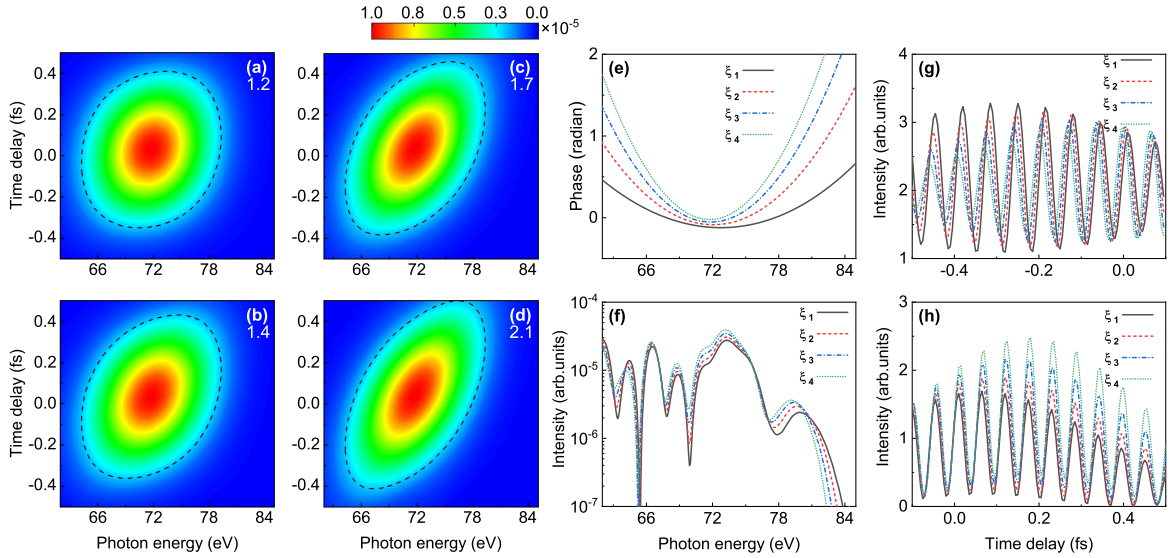

FIG. 6: The spectra of $|x_2^{\mathrm{EQRS}}(\omega,\tau)+x_3^{\mathrm{EQRS}}(\omega,\tau)|^2$ calculated by using the EQRS model with different spectral phases of the XUV pulse defined by the GDD (in atomic units): (a) ξ_1 = -0.006 (black full line), (b) ξ_2 = -0.012 (red dashed line), (c) ξ_3 = -0.018 (blue dot-dashed line), and (d) ξ_4 = -0.024 (green dotted line). Black dotted lines are the contour lines which indicate 20 % of the peak spectral intensity. (e) The phase of $x_2^{\mathrm{EQRS}}(\omega,\tau)+x_3^{\mathrm{EQRS}}(\omega,\tau)$ at zero time delay. (f) The HHG spectra by including the interference with $x_1^{\mathrm{QRS}}(\omega)$ at zero time delay. The streaking spectra versus the time delay at two fixed photon energies: (g) 62 eV and (h) 76 eV.

We first extract the relative group delay from the HHG streaking spectra. As shown in Figs. 5(b) and (c), the peaks of intensity signals at different energies are connected by straight lines, which help to extract the relative group delays as

$$\Delta G = \frac{\omega_1\tau_1 - \omega_2\tau_2}{\omega_1 - \omega_2}, \tag{24}$$

where τ_1 and τ_2 are the time delays where the peaks appear for ω_1 and ω_2, respectively. For the photon-energy region of 63.6-68.2 eV below the cutoff energy of E_c, the relative group delay is $\Delta G_{below} \approx$ 1.59 fs or -0.60 fs for the black line and the purple line, respectively. While $\Delta G_{above} \approx$ 0.49 fs for the photon energies of 72.9-77.5 eV above the cutoff energy.

We can also calculate $d\phi_1(\omega)/d\omega$ in Eq. (23) by using the semi-classical three-step model. The electric field of the IR pulse (black line) is plotted in Fig. 5 (d), and the harmonic emission times (red line) as a function of photon energy for both "short" and "long" trajectories are calculated by the classical model. For cutoff harmonics, "short" and "long" trajectories are merged. The spectral phase $\phi_1(\omega)$ can be obtained as

$$\phi_1(\omega) = \omega t_{IR}, \tag{25}$$

with t_{IR} being the harmonic emission time. For the photon energies of 63.3-68.2 eV, $d\phi_1(\omega)/d\omega$ is 2.11 fs and -1.03 fs for "short" and "long" trajectories, respectively, while it is 0.53 fs for cutoff harmonics in the photon-energy region of 72.9-77.5 eV.

From the agreement between ΔG extracted from the HHG streaking spectra and $d\phi_1(\omega)/d\omega$ calculated by the classical model, we can get the following conclusions. First, it confirms that the interference model based on the EQRS model is valid, in which the HHG streaking spectra are generated by the XUV pulse interferes with harmonics by the IR laser. Second, it can also be concluded that the strong (or weak) interference fringes [indicated by the black line (or the purple line) in Fig. 5(a)] in the HHG streaking spectra are caused by the interference between the XUV pulse and "short"-trajectory (or "long"-trajectory) harmonics. For the interference fringes above the cutoff energy, they are due to the interference between the XUV pulse and cutoff harmonics. Third, the interference fringes may be used to reconstruct the time-frequency picture of harmonic emission [43].

D. Retrieval of the XUV pulse with the HHG streaking spectra by the EQRS model

1. *Sensitivity of the HHG streaking spectra on the XUV spectral phase*

The HHG streaking spectra may be used to retrieve the XUV pulse, or more specifically, its spectral phase. We first need to check whether they are sensitive to the spectral phase of the XUV pulse. In the frequency domain, the XUV pulse can be expressed as $E_{XUV}(\omega) = U(\omega)e^{i\phi(\omega)}$, where $U(\omega)$ is the spectral amplitude and $\phi(\omega)$ is the spectral phase. We start with the same TL XUV pulse in Fig. 3. With the same $U(\omega)$, the phase $\phi(\omega)$ is given by $\phi(\omega) = \frac{\xi}{2}(\omega-\omega_c)^2$, where ω_c is the cen-

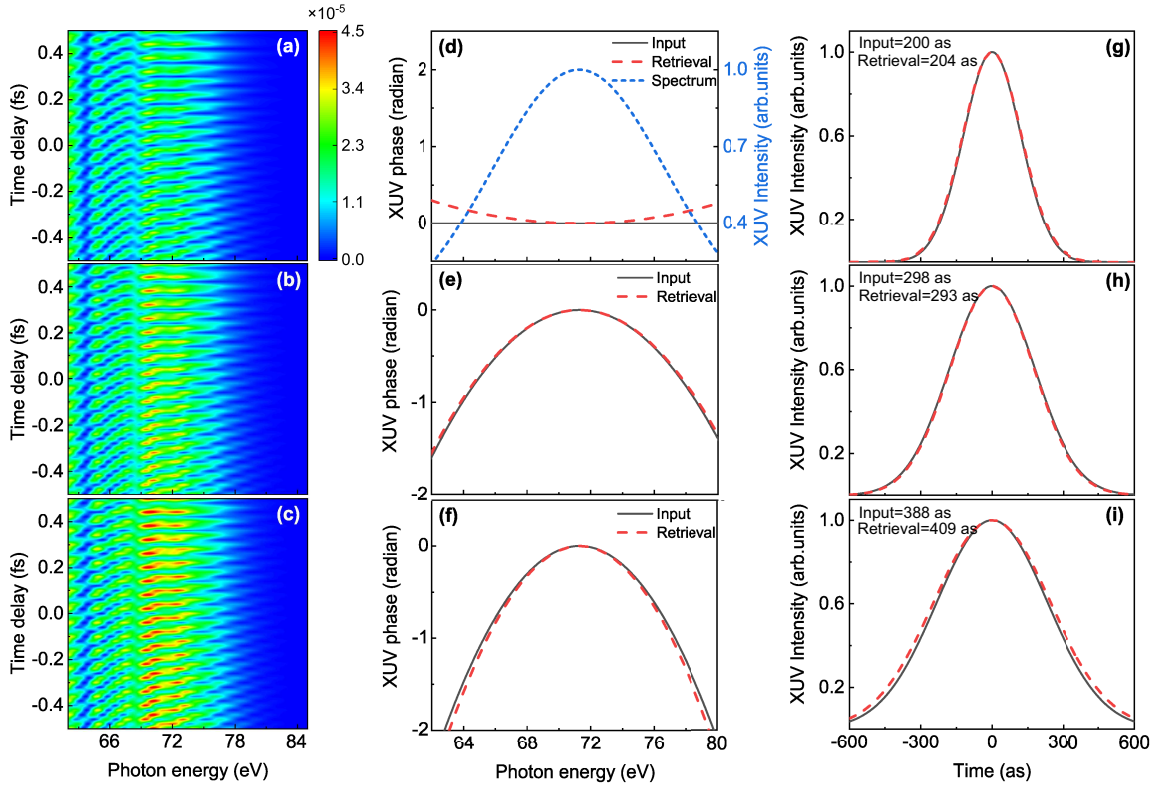

FIG. 7: Characterization of three XUV pulses centered at 71.3 eV with a bandwidth of 9 eV. The GDD coefficients ξ (in atomic units) of these XUV pulses are 0 (first row), -0.016 (second row), and -0.024 (third row), respectively. (a)-(c) The input modulated spectra simulated by the TDSE are treated as "experimental" data. (d)-(f) Comparison of the input and retrieved spectral phases. (g)-(i) Comparison of the input and retrieved XUV intensity profiles in time domain. (The black solid lines are the input data, while the red dash lines are retrieved results.) The spectral intensity $U(\omega)^2$ of the XUV pulse (blue dotted line) is assumed known, as shown in (d).

tral photon energy and ξ is the coefficient of the group delay dispersion (GDD). In the EQRS model, the term of $x_1^{\rm QRS}(\omega)$ doesn't depend on the XUV pulse, so we check XUV-dependent terms of $x_2^{\rm EQRS}(\omega,\tau)+x_3^{\rm EQRS}(\omega,\tau)$ for completeness. We choose four different values of ξ, and show the spectra of $|x_2^{\rm EQRS}(\omega,\tau)+x_3^{\rm EQRS}(\omega,\tau)|^2$ in Figs. 6(a)-(d) (the normalization factor is indicated in each frame). It can be clearly seen that the spectra are very sensitive to the spectral phase of XUV pulse. We further show the phase of $x_2^{\rm EQRS}(\omega,\tau)+x_3^{\rm EQRS}(\omega,\tau)$ in Fig. 6 (e) when the time delay is set as zero. And the phase of XUV-dependent terms changes rapidly with the XUV phase. We then include term of $x_1^{\rm QRS}(\omega)$, and check how the HHG streaking spectra varying with the XUV phase. In Fig. 6 (f), the spectra are shown at zero time delay for four different XUV phases. The spectra change dramatically with the spectral phase. Similarly, as shown in Figs. 6(g) and (h), the intensity of harmonics at two energies show rapid modulations versus the time delay with the period of about 58 as of the XUV pulse. These strong dependence on the spectral phase of the XUV makes the harmonic streaking spectra as a good candidate for retrieving the XUV spectral phase.

2. *Retrieval of the XUV pulse from the TDSE-based HHG streaking spectra*

In the following we describe a general procedure for retrieving the spectral phase of the XUV pulse from the HHG streaking spectra. First, the XUV pulse and IR laser are characterized by a set of parameters $\{a_1, a_2, ..., a_n\}$. Second, for given ranges of photon energy and time delay, a fitness function is defined as

$$F\{a_i\} = \frac{\sum_{k,l}[S_0(\omega_k,\tau_l) - S_1(\omega_k,\tau_l)]^2}{N_k N_l}, \qquad (26)$$

where S_0 are the input spectrograms and S_1 are the simulated spectra with the EQRS model by using one set of $\{a_1, a_2, ..., a_n\}$. N_k and N_l are the number of data points for the photon energy and the time delay, respectively. Third, the multiple parameters can be searched and determined by minimizing $F\{a_i\}$.

The purpose of this work is to demonstrate the applicability of the HHG streaking spectra for characterizing the XUV pulse. Since the IR laser alone is strong enough to generate high harmonics, it can be characterized independently with the generated HHG spectra. And the

spectral intensity of XUV pulse can be easily measured with spectrometer. We assume that the IR laser and the spectral intensity of the XUV are known, and the spectral phase is characterized by the GDD coefficient ξ, i.e., the XUV pulse is characterized by a single parameter. For different values of ξ, the HHG streaking spectra calculated by using the TDSE are shown in Figs. 7(a)-(c). The spectrograms are significantly changed by varying the XUV spectral phase. These data are used as "input" data, or "experimental" data that we want to fit. We then search the optimized ξ until $F\{a_i\}$ is minimized. In the retrieval procedure, we typically choose 100 points in the time delay and 300 points in the photon energy. The retrieved spectral phases are plotted (red dashed lines) in Figs. 7(d)-(f). For comparison, the input phases are also shown (black solid lines). To evaluate the accuracy of the retrieved results, we plot the XUV intensity profiles in time domain in Figs. 7(g)-(i). For the TL pulse, our method gives a pulse duration (FWHM) of 205 as in comparison with the input value of 200 as in Fig. 7(g). As the absolute values of ξ are increased, the retrieved (input) durations are 293 (298) as and 409 (388) as in Figs. 7(h) and (i), respectively. All input XUV pulse durations can be successfully retrieved with a relative error less than 5%.

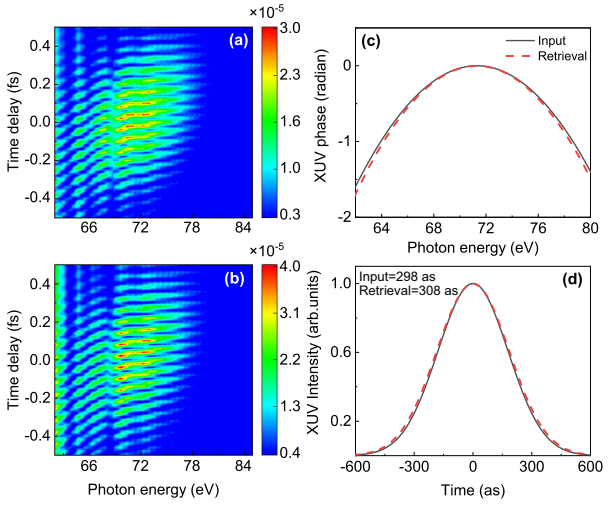

FIG. 8: (a) The HHG streaking spectra after accounting for the propagation effects by averaging IR intensities (input). The GDD coefficient ξ (in atomic units) is -0.016. (b) The retrieved modulation spectra by using the single-atom theory. Comparison of the retrieved XUV spectral phase (c) and the temporal intensity profile (d).

3. *Retrieval of XUV pulses from macroscopic HHG streaking spectra*

In the above retrieval procedure, the input data are taken from the single-atom response. In reality, the experimentally measured HHG spectra undergo change from the macroscopic phase-matching effects as the light emerges from the gas medium [59–66]. Our retrieval method needs to be checked with experimental HHG streaking spectra which depend on the focusing conditions. Instead of accounting for good phase matching when the gas medium is placed after the laser focus by solving the three-dimensional Maxwell's wave equation [67], an easier "shortcut" to get the same result is to average the single-atom complex harmonic amplitudes over a narrow intensity range. We have used such a simplified procedure by averaging over a range $[0.95I_c, 1.05I_c]$ around the central intensity I_c, where $I_c = 2.5 \times 10^{14}$ W/cm^2. Note that the average was taken coherently and the XUV pulse was not varied since its Rayleigh length is much longer than IR laser. The resulting "experimental" streaking HHG spectra are shown in Fig. 8(a). For simplicity, the S_1 in Eq. (26) are still given by the single-atom spectra calculated with the EQRS model. With the known XUV spectral intensity and the IR laser of intensity I_c, we use the same single-parameter retrieval method to obtain the XUV spectral phase, and thus the XUV pulse. Using the retrieved XUV pulse, we can calculate the streaking spectra, as shown in Fig. 8(b) which compares nicely to the "input" one shown in Fig. 8(a). The retrieved XUV spectral phase and temporal intensity profile are plotted in Figs. 8(c) and (d), respectively. The retrieved pulse duration is 308 as, which compares well to the input value of 298 as. This shows that macroscopic propagation of the harmonic spectra do not alter the essential features in the single-atom HHG streaking spectra.

IV. CONCLUSIONS

In summary, we have established an extended quantitative rescattering (EQRS) model to accurately and efficiently simulate the HHG streaking spectra generated by the combination of a linearly polarized weak XUV pulse with an intense IR laser. In this model, the induced dipole caused by the IR laser alone can be calculated by using the standard QRS model while the time-delay dependent IR-XUV coupling terms can be corrected by considering the contributions from the IR-laser ionization and the bound-continuum transition. The consistence of this model has been checked by treating the target atom as a hydrogenlike or a Gaussian atom in the SFA. The EQRS model has also been calibrated by comparing with the results obtained from the TDSE solutions. Next we have uncovered the physical mechanism of the fringes in the HHG streaking spectra, which are caused by the interference between the XUV pulse and harmonics by IR laser. The harmonics generated by the "short" or "long" electron trajectory or above the cutoff are responsible for interference fringes with the different slopes. Then we have examined that the HHG streaking spectra are sensitive to the XUV spectral phase, thus nicely forms the basis for the retrieval. Finally, we have demonstrated

that spectral phase of the XUV pulse can be retrieved with the present method by using "input" HHG spectra generated from solving the TDSE and the result remains the same even if the phase matching in the macroscopic gas medium is included.

In this work, the central photon energy of XUV pulse is only chosen to be far from the ionization threshold of target atom and the pulse duration about few hundreds of attoseconds. The applicability of EQRS model needs to be further checked for a wide parameter range of XUV pulse. Recently, with the development of laser technology in the mid-infrared, several groups have reported continuum harmonic spectra in the water-window or soft X-ray (SXR) region [68–71], it is also interesting to check whether the EQRS model can be used to simulate the HHG streaking spectra by the synchronization of attosecond SXR pulse and mid-infrared laser. In the present retrieval, we simulated the case where there is only one unknown parameter. If multiple parameters are required to characterize both the XUV pulse and IR laser, optimization algorithms [72, 73] should be applied to speed up the process for searching optimal parameters. In addition, the retrieval of a broadband soft X-ray IAP generated with mid-IR lasers is also appealing and the capability of present retrieval method will be explored in the future.

V. ACKNOWLEDGMENTS

This work was supported by National Natural Science Foundation of China (NSFC) under Grants No. 11774175, No. 91950102, and No. 11834004. C.D.L. was supported by Chemical Sciences, Geosciences and Biosciences Division, Office of Basic Energy Sciences, Office of Science, U. S. Department of Energy under Grant No. DE-FG02-86ER13491.

[1] A. McPherson, G. Gibson, H. Jara, U. Johann, T. S. Luk, I. A. McIntyre, K. Boyer, and C. K. Rhodes, J. Opt. Soc. Am. B **4**, 595 (1987).
[2] M. Ferray, A. LHuillier, X. F. Li, L. A. Lompre, G. Mainfray, and C. Manus, J. Phys. B, **21**, L31 (1988).
[3] F. Calegari, G. Sansone, S. Stagira, C. Vozzi, and M. Nisoli, J. Phys. B, **49**, 062001 (2016).
[4] L.-Y. Peng, W.-C. Jiang, J.-W. Geng, W.-H. Xiong and Q. Gong, Phys. Rep. **575**, 1 (2015).
[5] F. Krausz, M. Ivanov, Rev. Mod. Phys. **81**, 163 (2009).
[6] P. M. Paul, E. S. Toma, P. Breger, G. Mullot, F. Augé, P. Balcou, H. G. Muller, and P. Agostini, Science **292**, 1689 (2001).
[7] M. Hentschel, R. Kienberger, C. Spielmann, G. A. Reider, N. Milosevic, T. Brabec, P. Corkum, U. Heinzmann,M. Drescher, and F. Kraus, Nature **414**, 509 (2001)
[8] E. Goulielmakis, M. Schultze, M. Hofstetter, V. S. Yakovlev, J. Gagnon, M. Uiberacker, A. L. Aquila, E. M.Gullikson, D. T. Attwood, R. Kienberger, F. Krausz, and U. Kleineberg, Science **320**, 1614 (2008).
[9] A. Jullien, T. Pfeifer, M. J. Abel, P. M. Nagel, M. J. Bell, D. M. Neumark, and S. R. Leon, Appl. Phys. B **93**, 433 (2008).
[10] I. J. Sola, E. Mével, L. Elouga, E. Constant, V. Strelkov, L. Poletto, P. Villoresi, E. Benedetti, J. P. Caumes, S. Stagira, C. Vozzi, G. Sansone, and M. Nisoli, Nat. Phys. **2**, 319 (2006).
[11] H. Vincenti, and F. Quéré, Phys. Rev. Lett. **108**, 113904 (2012).
[12] K. T. Kim, C. M. Zhang, T. Ruchon, J. F. Hergott, T. Auguste, D. M. Villeneuve, P. B. Corkum, and F. Quéré, Nat. Photonics **7**, 651 (2013).
[13] S. W. Huang, G. Cirmi, J. Moses, K. H. Hong, S. Bhardwaj, J. R. Birge, L. J. Chen, E. Li, B. J. Eggleton, G. Cerullo, and F. X. Kärtner, Nat. Photonics **5**, 475 (2011).
[14] D. Greening, B. Weaver, A. J. Pettipher, D. J. Walke, E. W. Larsen, J. P. Marangos, and J. W. G. Tisch, Opt. Express **28**, 23329 (2020).
[15] E. J. Takahashi, P. F. Lan, O. D. Mücke, Y. Nabekawa, and K. Midorikawa, Nat. Commun. **4**, 2691 (2013).
[16] B. Xue, Y. Tamaru, Y. Fu, H. Yuan, P. F. Lan, O. D. Mücke, A. Suda, K. Midorikawa, and E. J. Takahas, Sci. Adv. **6**, eaay2802 (2020).
[17] Y. Pertot, C. Schmidt, M. Matthews, A. Chauvet, M. Huppert, V. Svoboda, A. von Conta, A. Tehlar, D. Baykusheva, J. P. Wolf, and H. J. Wörner, Science **355**, 264 (2017).
[18] A. Ozawa, J. Rauschenberger, C. Gohle, M. Herrmann, D. R. Walker, V. Pervak, A. Fernandez, R. Graf, A. Apolonski, R. Holzwarth, F. Krausz, T. W. Hänsch, and T. Udem, Phys. Rev. Lett. **100**, 253901 (2008).
[19] C. Buth, F. He, J. Ullrich, C. H. Keitel, and K. Z. Hatsagortsyan, Phys. Rev. A **88**, 033848 (2013).
[20] M. R. Miller, C. Hernández-García, A. Jaroń-Becker, and A. Becke, Phys. Rev. A **90**, 053409 (2014).
[21] C. Liu, Z. Zeng, R. Li, Z. Xu, and M. Nisoli, Opt. Express **23**, 9858 (2015).
[22] C. Figueira de Morisson Faria, P. Salières, P. Villain, and M. Lewenstein, Phys. Rev. A **74**, 053416 (2006).
[23] K. J. Schafer, M. B. Gaarde, A. Heinrich, J. Biegert, and U. Keller, Phys. Rev. Lett. **92**, 023003 (2004).
[24] G.-T. Zhang, J. Wu, C.-L. Xia, and X.-S. Liu, Phys. Rev. A **80**, 055404 (2009).
[25] A. Fleischer, Phys. Rev. A **78**, 053413 (2008).
[26] A. C. Brown and H. W. van der Hart, Phys. Rev. Lett. **117**, 093201 (2016).
[27] J.-A. You, J. M. Dahlström, and N. Rohringer, Phys. Rev. A **95**, 023409 (2017).
[28] N. B. Delone, N. L. Manakov, and A. G. Fainshtein, J. Exp. Theor. Phys. **59**, 529 (1984).
[29] M. Lewenstein, P. Balcou, M. Y. Ivanov, A. LHuillier, and P. B. Corkum, Phys. Rev. A **49**, 2117 (1994).
[30] T. S. Sarantseva, M. V. Frolov, and N. V. Vvedenskii, Quantum Electron. **48**, 625(2018).
[31] J. Seres, E. Seres, B. Landgraf, B. Ecker, B. Aurand, A. Hoffmann, G. Winkler, S. Namba, T. Kuehl, and C. Spielmann, Sci. Rep. **4**, 04254 (2014).
[32] C. Serrat, D. Roca, and J. Seres, Opt. Express **23**, 4867

(2015).
[33] C. Serrat, D. Roca, J. M. Budesca, J. Seres, E. Seres, B. Aurand, A. Hoffmann, S. Namba, T. Kuehl, and C. Spielmann, Opt. Express **24**, 8028 (2016).
[34] J. Seres, E. Seres, D. Hochhaus, B. Ecker, D. Zimmer, V. Bagnoud, T. Kuehl, and C. Spielmann, Nat. Phys. **6**, 455 (2010).
[35] J. Seres, E. Seres, and C. Spielmann, Phys. Rev. A **86**, 013822 (2012).
[36] C. Serrat, Phys. Rev. Lett. **111**, 133902 (2013).
[37] J. Seres, E. Seres, B. Landgraf, B. Ecker, B. Aurand, T. Kuehl, and C. Spielmann, Sci. Rep. **4**, 04234 (2014).
[38] C. Serrat, J. Seres, E. Seres, and S. Namba, Phys. Rev. A **99**, 063425 (2019).
[39] C. Serrat, Phys. Rev. A **93**, 063415 (2016).
[40] J. Xue, C. Liu, Y. Zheng, Z. Zeng, R. Li, and Z. Xu, Opt. Express **26**, 9243 (2018).
[41] T. S. Sarantseva, M. V. Frolov, N. L. Manakov, A. A. Silaev, A. A. Romanov, N. V. Vvedenskii, and A. F. Starace, Phys. Rev. A **101**, 013402 (2020).
[42] W. Dong, H. Hu, and Z. Zhao, Opt. Express **28**, 22490 (2020).
[43] T. S. Sarantseva, A. A. Silaev, A. A. Romanov, N. V. Vvedenskii and M. V. Frolov, Opt. Express **29**, 1428 (2021).
[44] A.-T. Le, R. R. Lucchese, S. Tonzani, T. Morishita, and C. D. Lin, Phys. Rev. A **80**, 013401 (2009).
[45] C. D. Lin, A.-T. Le, C. Jin, and H. Wei, J. Phys. B **51**, 104001 (2018).
[46] T. Morishita, A.-T. Le, Z. Chen, and C. D. Lin, Phys. Rev. Lett. **100**, 013903 (2008).
[47] A.-T. Le, T. Morishita, and C. D. Lin, Phys. Rev. A **78**, 023814 (2008).
[48] S.-F. Zhao, Y. Wang, G. Wang, and X.-X. Zhou, Opt. Commun. **328**, 30 (2014).
[49] A.-T. Le, R. D. Picca, P. D. Fainstein, D. A. Telnov, M. Lein, and C. D. Lin, J. Phys. B **41**, 081002 (2018).
[50] N. Abro, K. Wang, X. Zhu, B. Li, and C. Jin, Phys. Rev. A **98**, 023411 (2018).
[51] A. M. Perelomov, V. S. Popov, and M. V. Terentev, J. Exp. Theor. Phys. **23**, 924 (1966).
[52] M. V. Frolov, N. L. Manakov, T. S. Sarantseva, and A. F. Starace, J. Phys. B **42**, 035601 (2009).
[53] M. V. Frolov, N. L. Manakov, A. M. Popov, O. V. Tikhonova, E. A. Volkova, A. A. Silaev, N. V. Vvedenskii, and A. F. Starace, Phys. Rev. A **85**, 033416 (2012).
[54] Y. Okajima, O. I. Tolstikhin, and T. Morishita, Phys. Rev. A **85**, 063406 (2012).
[55] M. V. Frolov, N. L. Manakov, A. A. Minina, A. A. Silaev, N. V. Vvedenskii, M. Y. Ivanov, and A. F. Starace, Phys. Rev. A **99**, 053403 (2019).
[56] X. M. Tong, and C. D. Lin, J. Phys. B **38**, 2593 (2005).
[57] Y. Mairesse, A. de Bohan, L. J. Frasinski, H. Merdji, L. C. Dinu, P. Monchicourt, P. Breger, M. Kovačev, R. Taïeb, B. Carré, H. G. Muller, P. Agostini, and P. Salières, Science **302**, 1540 (2003).
[58] N. Dudovich, O. Smirnova, J. Levesque, Y. Mairesse, M. Y. Ivanov, D. M. Villeneuve, and P. B. Corkum, Nat. Phys. **2**, 781 (2006).
[59] I. P. Christov, M. M. Murnane, and H. C. Kapteyn, Phys. Rev. A **57**, R2285 (1998).
[60] E. Priori, G. Cerullo, M. Nisoli, S. Stagira, S. De Silvestri, P. Villoresi, L. Poletto, P. Ceccherini, C. Altucci, R. Bruzzese, and C. de Lisio, Phys. Rev. A **61**, 063801 (2000).
[61] M. Geissler, G. Tempea, and T. Brabec, Phys. Rev. A **62**, 033817 (2000).
[62] V. Tosa, H. T. Kim, I. J. Kim, and C. H. Nam, Phys. Rev. A **71**, 063807 (2005).
[63] V. S. Yakovlev, M. Ivanov, and F. Krausz, Opt. Express **15**, 15351 (2007).
[64] M. B. Gaarde, J. L. Tate, and K. J. Schafer, J. Phys. B **41**, 132001 (2008).
[65] C. Hernández-García, J. A. Pérez-Hernández, J. Ramos, E. C. Jarque, L. Roso, and L. Plaja, Phys. Rev. A **82**, 033432 (2010).
[66] C. Jin, A.-T. Le, and C. D. Lin, Phys. Rev. A **83**, 023411 (2011).
[67] C. Jin, A.-T. Le, and C. D. Lin, Phys. Rev. A **79**, 053413 (2009).
[68] F. Silva, S. M. Teichmann, S. L. Cousin, M. Hemmer, and J. Biegert, Nat. Commun. **6**, 6611 (2015).
[69] T. Gaumnitz, A. Jain, Y. Pertot, M. Huppert, I. Jordan, F. Ardana-Lamas, and H. J. Wörner, Opt. Express **25**, 27506 (2017).
[70] A. S. Johnson, D. R. Austin, D. A. Wood, C. Brahms, A. Gregory, K. B. Holzner, S. Jarosch, E. W. Larsen, S. Parker, C. S. Strüber, P. Ye, J. W. G. Tisch, and J. P. Marangos, Sci. Adv. **4**, eaar3761 (2018).
[71] Y. Fu, K. Nishimura, R. Shao, A. Suda, K. Midorikawa, P. Lan, and E. J. Takahashi, Commun. Phys. **3**, 92 (2020).
[72] X. Zhao, H. Wei, Y. Wu, and C. D. Lin, Phys. Rev. A **95**, 043407 (2017).
[73] C. Jin, G. Wang, H. Wei, A. T. Le, and C. D. Lin, Nat. Commun. **5**, 4003 (2014).